Supplementary Material for

Controlled Flight of a Biologically Inspired, Insect-Scale Robot

Kevin Y. Ma,* Pakpong Chirarattananon, Sawyer B. Fuller, Robert J. Wood

*Corresponding author. E-mail: kevinma@seas.harvard.edu

Published 3 May 2013, *Science* **340**, 603 (2013)
DOI: 10.1126/science.1231806

This PDF file includes:

Other Supplementary Material for this manuscript includes the following:
(available at www.sciencemag.org/cgi/content/full/340/6132/603/DC1)

Movies S1 and S2

Materials and Methods

1. Measurement and Interface

3D position and orientation data are captured with an infrared-based Vicon motion capture system (Vicon, Oxford, UK), consisting of eight Model-T40 cameras arranged to provide a tracking volume of 0.6x0.6x0.6 m. The system is capable of motion resolution of less than one millimeter and operates at 500 Hz. Four 1.5 mm-diameter retroreflective tracking markers (with their plastic cores removed for weight reduction) are adhered to the robotic fly to allow its rigid body dynamics to be tracked by the cameras. Image data is processed using the proprietary Vicon Tracker software to estimate position and orientation of the robot. This estimate is transmitted over serial RS-232 to a second computer performing control calculations.

The control computer is an xPC Target system (Mathworks, Natick, MA, USA), a software environment that runs MATLAB Simulink-designed controllers in hard real-time on a desktop microprocessor. The controller runs at 10 kHz for both input measurements and output control signals. An automatic switch-off routine is activated whenever the robotic fly moves out of the control volume or its body attitude exceeds 70°. The output control signals are converted from digital signals to analog signals with a range of 0V–3V. These analog signals are passed through a high voltage amplifier (Trek PZD350) with a 100X amplification factor, increasing the voltage range to 0V–300V, which is necessary to drive the piezoelectric bimorph flight muscles (*31*). A power tether then carries these input signals to the robotic fly. The power tether is a 0.6 meter long bundle of four 51-gauge, enamel-clad copper wires carrying a ground signal, a 300V voltage rail, and two drive signals.

The piezoelectric bimorphs are driven using the parallel, single-source drive technique as detailed in (*22*). The actuators are strain-limited by brittle fracture of the piezoelectric ceramic plates, and for the actuator geometry used in this work, we have empirically found the upper limit of the plates to be approximately 300V. The piezoelectric ceramic material in the flight muscles (PZT-5H from PiezoSystems) can sustain a maximum strain between 0.1% to 0.2%, depending on manufacturing process control. The typical strains that the material experiences during operation typically do not exceed approximately 0.08%.

1.1. Latency of the experimental setup

We attempt to estimate the latency of the experimental system, including the processing time of the motion capture system, communication latency between computing units, and any other effects, using a single, unloaded piezoelectric bimorph actuator. A retroreflective marker is attached to the tip for tracking deflection while it is driven with different sinusoid signals. The time difference between the command signal and the resultant motion estimated by the motion capture apparatus, after accounting for the time lag induced by the mechanical dynamics of the actuator, is estimated to be 8 milliseconds.

A model of the robot's actuator-transmission-wing system suggests that it can be approximated as a second order system (*28*). Near its resonant frequency, it is expected that the flapping motion would be no more than 180° out of phase with the driving

signals. This equates to a 4 milliseconds delay for the flapping frequency of 120 Hz. Thus in total, the latency of the experimental setup is approximately 12 milliseconds.

1.2. Power consumption estimates

Concerning onboard power, we measured power consumption of the robot to be 19 mW, suggesting that with an electrical conversion efficiency of 70% (*31*) and an assumed battery energy density of 0.5 kJ/g, a battery equal to the mass of the current robot would power flight for a few minutes. However, this is for idealized conditions and neglects the power consumption from other onboard components.

2. Commanded torques to wing trajectories

Previous work has shown that a quasi-steady blade-element aerodynamic model applied to a wing on a passive rotation flexure hinge, as used in our robot design, can accurately predict aerodynamic forces and moments generated by the wing (*23*). We use this simulation with our robot's wing parameters to estimate the stroke-averaged forces and torques as a function of the wing trajectory.

To generate the split-cycle signals that induce yaw torque (*30*) as illustrated in Figure 1, E and F, we add a second harmonic (at double the flapping frequency) to the nominally sinusoidal drive signal, creating an asymmetric stroke cycle (Fig. S1). We also scale the components appropriately to ensure that the wing stroke amplitude remains unchanged.

The aerodynamic model used above predicts negligible coupling between the torques, but they are coupled to the flapping amplitude and thus the propulsive force magnitude. For control purposes, we use the aerodynamic model to derive a simplified numerical linearization for the thrust force and the torques as a function of wing kinematics, as follows:

$$F_t = \alpha_t \psi - \beta_t$$
$$\tau_r = (\alpha_r \psi - \beta_r)\theta_r$$
$$\tau_p = (\alpha_p \psi - \beta_p)\theta_p$$
$$\tau_y = (\alpha_y \psi - \beta_y)\eta$$

where F_t represents the propulsive thrust force, ψ is the mean flapping amplitude, τ_i's are body torques along roll, pitch, and yaw axes, θ_r is the differential stroke amplitude between the two wings, θ_p is the shift in mean stroke angle, η is the relative proportion of the second-harmonic signal (used to generate yaw torques), and α_i's and β_i's are numerical constants arisen from the linearization.

Finally, the desired wing trajectories are mapped to input signals that drive the piezoelectric flight muscles using a second-order linear model as an approximation of the flight muscle-thorax-wing system (*28*).

3. Controller design

The body dynamics of the robotic fly are fast — based on the measured torque generation, the robot should be able to perform a 90° turns in less than 30 milliseconds

(*20*). To stabilize such dynamics, the controller must be considerably faster. We use a 10 kHz controller operating frequency — on the order of 100 times faster than the nominal 120 Hz flapping frequency to obtain sufficiently smooth signals that avoid exciting a 1 kHz resonant mode in the actuators.

Complicating the control problem, we observe considerable, unpredictable variations from robot to robot due to small manufacturing differences that are difficult to characterize. To date, we have not found a commercially-available sensor with a suitable range (≈ 1–10 μNm), resolution (≈ 10 nNm), and possessing multiple, simultaneous measurement axes. A custom, dual-axis force-torque sensor capable of measuring a single axis of torque and a single force perpendicular to the torque axis of suitable range was demonstrated and used to measure thrust force magnitudes from the robot (*20*). Because there is no closed-form solution to the Navier-Strokes equations for flapping-wing flight, we must use approximations of the various features of the aeromechanical system to create a simple plant model. The rigid body dynamics in three-dimensional space are also markedly nonlinear. The combination of these uncertainties and the rapid dynamics of the system presents a challenging control problem.

The approach we are using here initially is to focus on achieving stable hovering behavior, dividing the controller into three modules: attitude, lateral position, and altitude controllers as described below. The overall architecture of the flight controller is schematically shown in Figure S2.

3.1. Attitude Controller

For the purposes of hovering, it is not necessary for the robotic fly to maintain a specific yaw angle heading because the robot can roll or pitch to move laterally in any direction. However, our attitude controller applies a damping effect to counteract rotation because otherwise, the slight fabrication asymmetries between the two wings results in rapid spinning behavior that destabilizes the robot.

A few assumptions regarding the dynamics of the robot are made to simplify the attitude controller design. First, the robot is treated as a rigid body, neglecting the inertial effects of the mass of the wings. Second, because we want stationary hovering, we assume the wind strength and translational and rotational velocities are near zero, so that we can neglect aerodynamic forces and torques arising from translational and rotational motions of the robot.

Accordingly, we can model the control problem as applying forces and torques to stabilize a simple rigid body under the influence of gravity alone. The attitude controller stabilizes the body in 3-D space using an energy-based Lyapunov function, motivated by (*32*). The function takes the form:

$$V_0 = k_p(1-\cos\phi) + \frac{1}{2}\omega^T I\omega,$$

where k_p is a positive scalar, I is the rigid body inertia matrix in the body coordinate frame, ω is the angular velocity, and ϕ is defined as the angle between the current body axis orientation ($\hat{z}$) and the desired body axis orientation ($\hat{z}_d$) such that

$\hat{z} \cdot \hat{z}_d = \cos\phi.$

The proposed Lyapunov function is a positive definite function and is zero only when the robot is oriented in the desired orientation with zero angular velocity. Assuming $\hat{z}_d$ is constant or slowly varying, the time derivative of the function is given by

$$\dot{V}_0 = k_p \omega^T \left(\begin{bmatrix} R_{12} & R_{22} & R_{32} \\ -R_{11} & -R_{21} & -R_{31} \\ 0 & 0 & 0 \end{bmatrix} \begin{bmatrix} \hat{z}_{d1} \\ \hat{z}_{d2} \\ \hat{z}_{d3} \end{bmatrix} \right) + \omega^T \tau ,$$

where R_{ij} represents an element in the rotation matrix describing the current orientation of the robot, $\hat{z}_{di}$ is the i^{th} element of the vector $\hat{z}_d$, and τ is the command torque vector to be generated by the robot. It follows that, for a positive constant k_v, the following control law

$$\tau = -k_p \left(\begin{bmatrix} R_{12} & R_{22} & R_{32} \\ -R_{11} & -R_{21} & -R_{31} \\ 0 & 0 & 0 \end{bmatrix} \begin{bmatrix} \hat{z}_{d1} \\ \hat{z}_{d2} \\ \hat{z}_{d3} \end{bmatrix} \right) - k_v \omega$$

yields

$\dot{V}_0 = -k_v \omega^T \omega \leq 0.$

According to the invariant set theorem, the system is globally asymptotically stable with zero attitude error and zero angular velocity under the assumptions given above.

In practice, however, angular velocity feedback is not directly available from the motion capture system. To ensure that the stability condition is retained, the Lyapunov function is modified with an additional term:

$$V = k_p (1 - \cos\phi) + \frac{1}{2} \omega^T I \omega + \frac{1}{2} k_v \chi^T \chi ,$$

where the dynamics of χ is described by

$$\chi = \frac{s}{s + \lambda} e.$$

Here s is a Laplace variable, λ is a positive constant, and e is a 3×1 vector containing Euler angles representing the orientation of the robot. There exists a matrix $E(e)$ that maps $\dot{e}$ to the angular velocity as

$\dot{e} = E(e)\omega.$

By using the control law

$$\tau = -k_p \left(\begin{bmatrix} R_{12} & R_{22} & R_{32} \\ -R_{11} & -R_{21} & -R_{31} \\ 0 & 0 & 0 \end{bmatrix} \begin{bmatrix} \hat{z}_{d1} \\ \hat{z}_{d2} \\ \hat{z}_{d3} \end{bmatrix} \right) - k_v E^T(e)\chi,$$

the time derivative of the Lyapunov function is given by

$$\dot{V}_0 = -k_v \chi^T \chi - k_v \omega^T E^T \chi + k_v \chi^T \dot{e}$$
$$= -\lambda k_v \chi^T \chi \leq 0.$$

Subsequently, the global asymptotic stability is achieved without directly using the angular velocity feedback. The resultant control law has a structure similar to a PD controller — the first term corresponds to a proportional error and the second term can be regarded as a derivative error. The values of k_p, k_v, and λ are experimentally tuned.

3.2. Lateral Controller

To navigate the robotic fly toward setpoint lateral positions, the lateral controller determines a desired body attitude of the robot ($\hat{z}_d$). By commanding tilt angles, the lateral controller controls lateral thrust forces. This desired attitude orientation is inputted to the attitude controller, which acts to regulate attitude to this new orientation. The magnitude of the lateral force is a function of the deviation angle between the instantaneous body axis and the vertical axis. This controller module is a proportional-derivative controller of the form:

$$\begin{bmatrix} \hat{z}_{d1} \\ \hat{z}_{d2} \end{bmatrix} = -k_{pl} \begin{bmatrix} X - X_d \\ Y - Y_d \end{bmatrix} - k_{vl} \begin{bmatrix} \dot{X} - \dot{X}_d \\ \dot{Y} - \dot{Y}_d \end{bmatrix},$$

where X, X_d, Y, Y_d are positions and desired positions, and k_{pl} and k_{vl} are controller gains. $\hat{z}_{d3}$ is calculated such that the magnitude of the vector $\hat{z}_d$ is unity. Additionally, a saturation scheme is implemented to ensure that the setpoint attitude does not deviate by more than 30° from the upright orientation.

3.3. Altitude Controller

The altitude controller determines the amount of propulsive force required to reach an altitude setpoint. It is a proportional-derivative controller, with a feedforward term to account for the gravity, and assumes a one-dimensional, upright oriented system.

Because we do not attempt rapid flight maneuvers requiring extreme body attitude angles, the altitude controller is designed to ignore the attitude of the robotic fly. It assumes the system is always upright, adjusting propulsive force magnitude to modulate vertical lift force and consequently vertical position. The approximation, which amounts to a linearization about an operating point at hover, holds because, in practice, the robotic fly rarely tilts more than 30° to generate lateral forces for lateral position control. The small deviation from vertical of the propulsive force vector only marginally disrupts the vertical lift force component.

Assuming a nearly upright orientation offers two beneficial consequences. First, it avoids commanding an increase in thrust when the robotic fly tilts from the upright orientation, leaving more voltage adjustment range to the more critical attitude controller (voltage range is limited by the voltage rail at 300V). Second, it reduces the amount of lateral drift that would arise if the robot increases thrust to compensate for off-axis tilting away from the upright orientation.

3.4. Compensation for torque biases from manufacturing variations

Open-loop experiments are performed prior to the closed-loop flights in order to identify input signals that minimize bias torques and approximate an operating state where there is zero body torque. These bias torques are the result of inevitable asymmetries due to manufacturing variations. The asymmetries offset the net propulsive thrust vector from the robot's center of mass, causing undesired residual torques about the body. This open-loop "trimming" procedure provides a rough estimate of the zero-body-torque state and is sufficient information to achieve short, marginally stable hovering flights. However, we find that the robotic fly steadily drifts laterally out of the control volume due to estimation inaccuracy. To achieve stable, stationary hovering, we compensate for the error by adding an integral term in the attitude controller to achieve zero-body-torque operation at steady-state. A secondary issue is that the zero-body-torque state does not necessarily coincide with the propulsive force vector of the robot oriented vertically, contributing additional lateral drift. We implement an algorithm in the lateral controller to evaluate the direction of the misaligned propulsive thrust vector and redefine the zero-body-torque state to remove the misalignment. This is carried out by considering a simplified model of the lateral dynamics of the robot, assuming steady hover (i.e. when lift thrust balances the gravitational force):

$$mg\begin{bmatrix} R_{13} \\ R_{23} \end{bmatrix} + mg\begin{bmatrix} r_X \\ r_Y \end{bmatrix} = m\begin{bmatrix} \ddot{X} \\ \ddot{Y} \end{bmatrix} + b\begin{bmatrix} \dot{X} \\ \dot{Y} \end{bmatrix},$$

where g is the gravitational constant, b is an aerodynamic drag coefficient, R_{13} and R_{23} are elements of a rotation matrix, and r_X and r_Y represent the misalignment of the body axes along the inertial coordinate frames. Here r_X and r_Y are determined using filtered derivatives on X and Y and projected back onto the robot's body frame. They are continuously estimated using a low-pass filter. A revised rotational matrix corresponding to the observed dynamics is then obtained. This is found to be sufficient to achieve the degree of lateral stability shown in Figure 2.

3.5. Effect of the tether wires

While difficult to quantify, we believe the tether wires have an insignificant, or at worse small, destabilizing effect on the dynamics of the robot for the following reasons. While hovering at an altitude of 10 cm, the robotic fly lifts off the ground approximately 10 cm of tether weighing less than 5 mg. This is less than 10% of the robot's body mass and easily compensated for by the altitude controller. Based on observations from the videos, the wires have a small amount of stiffness and thus extend laterally a small distance before hanging downward. This distance is typically within 3 cm of the body of the fly. In this configuration, it is anticipated that the torque contribution due to the mass of the

wire is on the order of 0.15 μNm, considerably smaller than the magnitude of commanded torques as shown in Figure 4. Additionally, due to the widely varying conformation of the wires as the fly performs lateral motions of more than 20 cm while only 10 cm off the ground, as can be seen in Videos S1 and S2, it is unlikely that the tether wires provided any consistent stabilizing effects. We treat the effect of the tether as a disturbance that is compensated for in the open-loop trimming experiments described in Section 3.4 and by the controller described in Sections 3.1, 3.2, and 3.3.

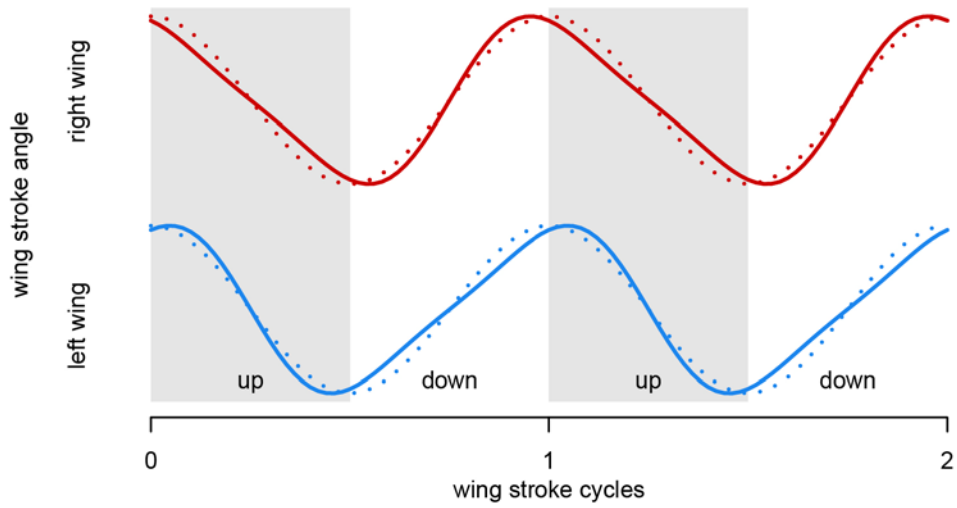

Fig. S1.

Plots illustrating the difference between a nominally sinusoidal input signal and the split-cycle input signals used to generate yaw torques. The relationship between the left and right wings' signals is illustrated. Split-cycle drive biases the peaks of the nominally sinusoidal signal by adding a second harmonic to the sinusoid. Here the dotted lines describe the nominal sinusoid and the solid line describes the split-cycle signal.

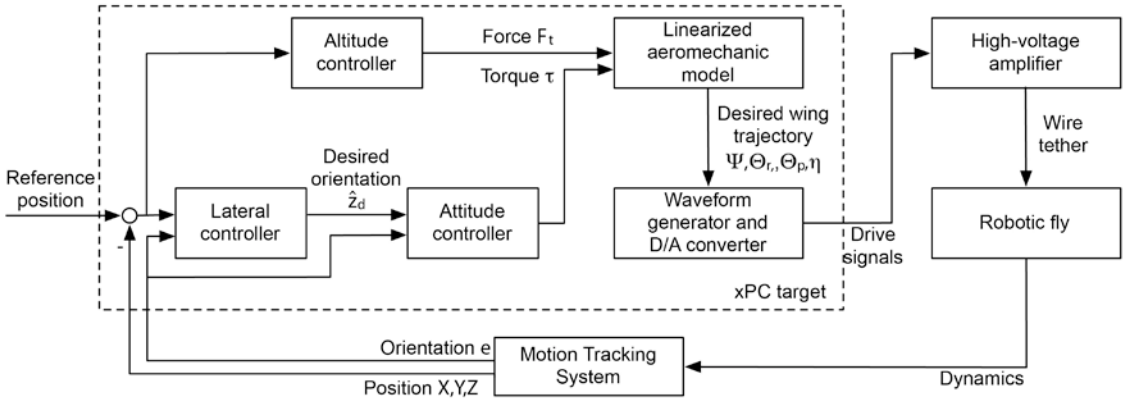

Fig. S2

Block diagram illustrating the control architecture. The controller contains three modules to control attitude, lateral position, and altitude. The calculated control forces and torques are converted first to wing trajectories and then to input signals for the robotic fly. The body dynamics of the robot are measured using a 3D motion tracking system.

Wing properties		
Wing length	15	mm
Mean chord length	3.46	mm
Area	52	mm^2
Inertia (flapping axis)	45.3	$mg \cdot mm^2$
Mass	1	mg
Robot properties		
Total robot mass	80	mg
Total flight muscle mass (2x muscles)	50	mg
Total tracking marker mass (4x markers)	5	mg
Wire tether mass (per 10 cm length)	5	mg
Roll axis inertia	1.42	$g \cdot mm^2$
Pitch axis inertia	1.34	$g \cdot mm^2$
Yaw axis inertia	0.45	$g \cdot mm^2$
Reynolds number	<1200	
Flapping frequency	120	Hz
Flapping amplitude	110	degrees
Power consumption (during hover)	19	mW
Robot geometry		
Height	14	mm
Body width	3.5	mm
Wing span	35	mm

Table S1.
Table of various physical parameters of the robotic fly.

Video S1

Video of the robotic fly performing a stationary hovering flight for 10 seconds at an altitude of 10 cm. The first segment is filmed at real-time speed. The second segment shows the same flight played back at 0.12X real-time speed, from high-speed footage filmed at 500 frames per second. A US quarter dollar is shown for scale.

Video S2

Video of the robotic fly performing lateral maneuvers. The setpoint position is switched between two points that are 20 cm apart and 10 cm in altitude. Two cycles are performed with a total flight time of 17 seconds. The first segment is filmed at real-time speed. The second segment shows the same flight played back at 0.18X real-time speed, from high-speed footage filmed at 500 frames per second. A US quarter dollar is shown for scale.

References and Notes

1. R. Dudley, *The Biomechanics of Insect Flight: Form, Function, Evolution* (Princeton Univ. Press, Princeton, NJ, 2002).

2. G. K. Taylor, Mechanics and aerodynamics of insect flight control. *Biol. Rev. Camb. Philos. Soc.* **76**, 449 (2001). doi:10.1017/S1464793101005759 Medline

3. G. Taylor, H. Krapp, Sensory systems and flight stability: What do insects measure and why? *Adv. Insect Physiol.* **34**, 231 (2007). doi:10.1016/S0065-2806(07)34005-8

4. C. Orlowski, A. Girard, Dynamics, stability, and control analyses of flapping wing micro-air vehicles. *Prog. Aerosp. Sci.* **51**, 18 (2012). doi:10.1016/j.paerosci.2012.01.001

5. M. H. Dickinson, F. O. Lehmann, S. P. Sane, Wing rotation and the aerodynamic basis of insect flight. *Science* **284**, 1954 (1999). doi:10.1126/science.284.5422.1954 Medline

6. R. Wood *et al*., Progress on 'pico' air vehicles. *Int. J. Robot. Res.* **31**, 1292 (2012). doi:10.1177/0278364912455073

7. C. P. Ellington, The novel aerodynamics of insect flight: Applications to micro-air vehicles. *J. Exp. Biol.* **202**, 3439 (1999). Medline

8. W. Trimmer, Microrobots and micromechanical systems. *Sens. Actuators* **19**, 267 (1989). doi:10.1016/0250-6874(89)87079-9

9. R. Wood, S. Avadhanula, R. Sahai, E. Steltz, R. Fearing, Microrobot design using fiber reinforced composites. *J. Mech. Des.* **130**, 052304 (2008). doi:10.1115/1.2885509

10. S. N. Fry, R. Sayaman, M. H. Dickinson, The aerodynamics of free-flight maneuvers in *Drosophila*. *Science* **300**, 495 (2003). doi:10.1126/science.1081944 Medline

11. A. Ennos, The kinematics and aerodynamics of the free flight of some *Diptera*. *J. Exp. Biol.* **142**, 49 (1989).

12. A. Ennos, The inertial cause of wing rotation in *Diptera*. *J. Exp. Biol.* **140**, 161 (1988).

13. M. Dickinson, M. Tu, The function of Dipteran flight muscle. *Comp. Biochem. Physiol. A* **116**, 223 (1997). doi:10.1016/S0300-9629(96)00162-4

14. M. H. Dickinson, Haltere-mediated equilibrium reflexes of the fruit fly, *Drosophila melanogaster*. *Philos. Trans. R. Soc. Lond. B Biol. Sci.* **354**, 903 (1999). doi:10.1098/rstb.1999.0442 Medline

15. L. Ristroph *et al*., Discovering the flight autostabilizer of fruit flies by inducing aerial stumbles. *Proc. Natl. Acad. Sci. U.S.A.* **107**, 4820 (2010). doi:10.1073/pnas.1000615107 Medline

16. C. T. David, The relationship between body angle and flight speed in free-flying *Drosophila*. *Physiol. Entomol.* **3**, 191 (1978). doi:10.1111/j.1365-3032.1978.tb00148.x

17. J. M. Zanker, On the mechanism of speed and altitude control in *Drosophila melanogaster*. *Physiol. Entomol.* **13**, 351 (1988). doi:10.1111/j.1365-3032.1988.tb00485.x

18. A. J. Bergou, L. Ristroph, J. Guckenheimer, I. Cohen, Z. J. Wang, Fruit flies modulate passive wing pitching to generate in-flight turns. *Phys. Rev. Lett.* **104**, 148101 (2010). doi:10.1103/PhysRevLett.104.148101 Medline

19. R. Wood, The first takeoff of a biologically inspired at-scale robotic insect. *IEEE Trans. Robot.* **24**, 341 (2008). doi:10.1109/TRO.2008.916997

20. K. Ma, S. Felton, R. Wood, "Design, fabrication, and modeling of the split actuator microrobotic bee," 2012 IEEE/RSJ International Conference on Intelligent Robots and Systems, Vilamoura, Algarve, Portugal, 7–12 October 2012, pp. 1133–1140.

21. M. Karpelson, G. Wei, R. Wood, "A review of actuation and power electronics options for flapping-wing robotic insects," 2008 IEEE International Conference on Robotics and Automation Pasadena, CA, USA, 19–23 May 2008, pp.779–786.

22. R. Wood, E. Steltz, R. Fearing, Optimal energy density piezoelectric bending actuators. *Sens. Actuators A Phys.* **119**, 476 (2005). doi:10.1016/j.sna.2004.10.024

23. J. Whitney, R. Wood, Aeromechanics of passive rotation in flapping flight. *J. Fluid Mech.* **660**, 197 (2010). doi:10.1017/S002211201000265X

24. D. L. Altshuler, W. B. Dickson, J. T. Vance, S. P. Roberts, M. H. Dickinson, Short-amplitude high-frequency wing strokes determine the aerodynamics of honeybee flight. *Proc. Natl. Acad. Sci. U.S.A.* **102**, 18213 (2005). doi:10.1073/pnas.0506590102 Medline

25. Materials and methods are available as supplementary materials on *Science* Online.

26. B. Cheng, X. Deng, T. L. Hedrick, The mechanics and control of pitching manoeuvres in a freely flying hawkmoth (*Manduca sexta*). *J. Exp. Biol.* **214**, 4092 (2011). doi:10.1242/jeb.062760 Medline

27. M. Abzug, E. Larrabee, *Airplane Stability and Control: A History of the Technologies that Made Aviation Possible* (Cambridge Univ. Press, Cambridge, UK, 2005).

28. B. Finio, N. Pérez-Arancibia, R. Wood, "System identification and linear time-invariant modeling of an insect-sized flapping-wing micro air vehicle," 2011 IEEE/RSJ International Conference on Intelligent Robots and Systems, San Francisco, CA, USA, 25–30 September 2011, pp. 1107–1114.

29. W. Hoburg, R. Tedrake, System identification of post stall aerodynamics for UAV perching. *Proc. AIAA Infotech Aerospace Conf.* (AIAA, Seattle, WA, 2009).

30. M. Oppenheimer, D. Doman, D. Sigthorsson, Dynamics and control of a biomimetic vehicle using biased wingbeat forcing functions: Part I — aerodynamic model. *Proc. 48th AIAA Aerospace Sci. Meeting* (AIAA, Orlando, FL, 2010).

31. M. Karpelson, G. Wei, R. Wood, Milligram-scale high-voltage power electronics for piezoelectric microrobots. *Proc. IEEE Int. Conf. Robotics Automation* (IEEE, Kobe, Japan, 2009), pp. 2217–2224.

32. F. Lizarralde, J. Wen, Attitude control without angular velocity measurement: A passivity approach. *IEEE Trans. Automat. Contr.* **41**, 468 (1996). doi:10.1109/9.486654